Significance of tissue anisotropy in optical tomography of the infant brain

Juha Heiskala, Tuomas Neuvonen, P. Ellen Grant, and Ilkka Nissilä

We study the effect of tissue anisotropy in optical tomography of neonates. A Monte Carlo method capable of modeling photon migration in an arbitrary 3D tissue model with spatially varying optical properties and tissue anisotropy is used for simulating measurements of neonates. Anatomical and diffusion tensor magnetic resonance imaging of neonates are used for creating the anatomical models. We find that tissue anisotropy affects the measured signal and the pattern of sensitivity in optical measurements. © 2007 Optical Society of America

OCIS codes: 170.5280, 170.6960.

1. Introduction

Diffuse optical tomography (DOT) is an emerging noninvasive medical imaging modality that uses near-infrared light to probe tissues. By finding the internal absorption and scattering properties of tissue, information about the anatomy and physiology of the tissue can be obtained. Due to the relatively strong and wavelength-dependent absorption of near-infrared light by oxygenated and deoxygenated hemoglobin, DOT is especially useful for observing changes in blood volume and oxygenation.

To draw information from optical measurements, light propagation through the tissue needs to be modeled. The radiative transfer equation (RTE) is a commonly used reference model to describe the propagation of near-infrared light, but solving it deterministically is complicated, and numerical implementations are computationally demanding. Near-infrared light is strongly scattered by most human tissues, which makes the propagation of light diffusive. Therefore the diffusion approximation (DA) to the RTE predicts the radiation propagation reasonably well in many cases. Methods based on the DA can be efficient and are widely used.[1] However, in some tissues, such as the cerebrospinal fluid (CSF), the DA yields inaccurate results. A more accurate result can be obtained using higher-order approximations to the RTE or the RTE itself. Monte Carlo (MC) methods are capable of solving the RTE without the need for approximations and are relatively easy to implement.

The effect of anisotropic structures that affect the propagation of near-infrared photons according to their direction is a potential issue. Such structures have been experimentally shown to cause direction dependence of light propagation in cases of chicken breast tissue, human skin, and dentin.[2–4] Modeling of anisotropic light propagation has been previously studied by Heino *et al.*,[5] Dagdug *et al.*,[6] and Heiskala *et al.*[7] The theoretical considerations have usually concentrated on developing ways to model the anisotropic propagation of radiation, and less emphasis has been put on exploring the implications of anisotropic effects in realistic measurement geometries.

In a previous study,[7] the authors developed a method for modeling anisotropic light propagation and created geometrically realistic models for the anisotropy using diffusion tensor (DT) magnetic resonance imaging (MRI). We applied our anisotropic MC

J. Heiskala (juha.heiskala@iki.fi) is with the BioMag Laboratory and T. Neuvonen is with the Department of Clinical Neurophysiology, Helsinki University Central Hospital, P.O. Box 340, HUS, FIN-00029, Helsinki, Finland. J. Heiskala and T. Neuvonen are also with the Helsinki Brain Research Center, University of Helsinki, P.O. Box 13, FIN-00014, Helsinki, Finland. J. Heiskala is also with the Laboratory of Biomedical Engineering, Helsinki University of Technology, P.O. Box 2200, FIN-02015 HUT, Finland. T. Neuvonen is also with the Department of Physiology, Neuroscience Unit, Institute of Biomedicine, University of Helsinki, P.O. Box 63, FIN-00014, Helsinki, Finland. P. E. Grant is with the Department of Pediatric Radiology, Massachusetts General Hospital, Boston, Massachusetts 02114. I. Nissilä, as well as P. E. Grant, is with the Athinoula A. Martinos Center for Biomedical Imaging, Massachusetts General Hospital, 149 13th Street, Charlestown, Massachusetts 02129.

model to the case of reflection geometry typically used for adult subjects and found the effects of anisotropy in this type of measurement to be very small.

Imaging of newborn full-term and preterm infants is an important potential application of near-infrared imaging because other imaging methods, such as MRI, are much more stressful to the infant, and currently no accurate bedside monitor of cerebral health exists. Also, because of the small size of the head and the thin skull, imaging deep-lying tissues is possible. Because measurements on infants are more sensitive to the deeper tissues of the brain than measurements on adults, and since the cortex of the premature brain is anisotropic,[8] tissue anisotropy can be expected to have greater significance.

2. Methods

We studied the effect of tissue anisotropy in optical imaging of the infant head by MC simulations using our anisotropic MC method described in Ref. 7. The anatomical models were obtained using MRI. The tissue types of each volume element (voxel) were derived from segmented T1-weighted images, and literature values of optical parameters[9] were assigned to the tissue types. The anisotropy data were obtained from DT images.

A. Monte Carlo Method

In the MC method of modeling light propagation, the routes of individual photon packets are traced in order to obtain the radiation distribution. The scattering and absorption of the photon flux are calculated based on the local optical properties in the tissue model. The reader is referred to previous publications[7,10–12] for details on the method.

In our MC implementation,[7] the tissue is divided into voxels, each of which may have different optical properties.[12] The optical properties of the model include absorption and scattering coefficients μ_a and μ_s, a bias factor g determining the directional bias of scattering, and the index of refraction n. We assume tissue anisotropy to make the scattering probability of the photons dependent on their propagation direction.[7] This is done by replacing the scattering coefficient μ_s by $\mu_{s,\text{iso}}\hat{\mathbf{s}}^T\mathbf{M}_s\hat{\mathbf{s}}$, where $\hat{\mathbf{s}}$ is the unit vector of the direction in which the photon is traveling, $\mu_{s,\text{iso}}$ is the isotropic scattering coefficient and the 3×3 tensor $\mathbf{M}_s$ describes the directional dependence of scattering.[7]

The effects of anisotropy on the sensitivity of the measurements to different regions of the imaged volume are an important consideration from a practical point of view, since it gives an idea of how large the errors are that are introduced into the results obtained by difference imaging if anisotropic effects are ignored. We calculated the sensitivity as the rate of change in the measured intensity in response to an infinitesimal change in absorption or scattering in the voxel

$$\frac{\partial A_{s,d}}{\partial \mu_{a,r}}, \qquad \frac{\partial A_{s,d}}{\partial \mu_{s,r}}, \tag{1}$$

where A is the measured intensity from source s to detector d, $\mu_{a,r}$ and $\mu_{s,r}$ are the absorption and scattering coefficients in voxel r, respectively. These partial derivatives can be calculated from the formula used in perturbation MC for small perturbations in μ_a and μ_s.[13–15] The formula, given below, yields the ratio of the perturbed amplitude contribution of a photon pack $\hat{A}$ and original amplitude contribution A when μ_a and μ_s in the perturbed region are changed into their perturbed values $\hat{\mu}_a$ and $\hat{\mu}_s$. j is the number of scattering events in the perturbed region, and L is the path length traveled by the photon pack in the perturbed region:

$$\hat{A}/A = \left(\frac{\hat{\mu}_s}{\mu_s}\right)^j \exp[-(\hat{\mu}_t - \mu_t)L], \qquad \mu_t = \mu_a + \mu_s. \tag{2}$$

By differentiating the above formula, we get

$$\frac{\partial \hat{A}}{\partial \hat{\mu}_a} = -L\hat{A}, \tag{3}$$

$$\frac{\partial \hat{A}}{\partial \hat{\mu}_s} = \left(-L + j\hat{\mu}_s^{-1}\right)\hat{A}. \tag{4}$$

When the average partial photon path length in a region of the imaged volume for a source–detector pair is known, Eqs. (3) and (4) can be used to calculate the sensitivity of the measurement to changes in absorption and scattering coefficients in that region. As can be seen from the equations, the unit of sensitivity is that of length (millimeter, when μ_s and μ_a are given in mm^{-1}).

Because changes in the circulation of blood in the brain mainly cause a change in the μ_a parameter, we consider only the sensitivity to $\Delta\mu_a$ here. However, since sensitivity of measurement to a region depends on the probability of photons traveling through the region from the source optode to the detector optode for both μ_a and μ_s, the sensitivity pattern will be very similar for the two parameters.

B. Anatomical Data

Anatomical data were derived from T1-weighted and DT-MR images of two neonates. The data were collected using a 1.5 Tesla Signa Scanner by GE Medical Systems.[16] The T1-weighted imaging was performed using a 256×192 acquisition matrix, a field of view of 220 mm $\times$ 165 mm, and a slice thickness of 1.5 mm. The diffusion tensor imaging was performed using a single-shot, echo-planar sequence with six gradient directions, a repetition time of 7500 ms, and time to echo of 101 ms. An acquisition matrix of 128×128 pixels, a field of view of 20 cm $\times$ 20 cm, and three signal averages were used. Twenty-three slices with slice thicknesses of 4 mm were obtained in the case of the first infant, and 19 slices with slice thicknesses of 5 mm were obtained in the case of the second infant. Slices of the T1-weighted and DT im-
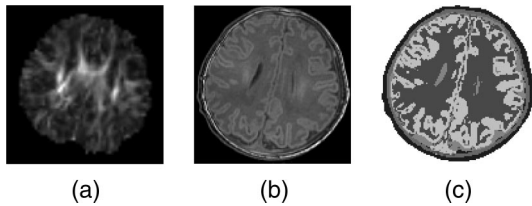
Fig. 1. Slices of DT and T1 data along with the segmentation of the T1 data. (a) FA index calculated from the DT data. (b) T1-weighted anatomical MR image. (c) Segmentation of the T1-weighted image.

ages along with the segmentation of the T1 image are shown in Fig. 1. The diffusion tensor data are represented by the fractional anisotropy (FA) index,[17] which describes the strength of the anisotropy. The head models studied were scaled by a factor of 0.7 so that their size corresponded to a preterm infant on which it is feasible to do full transmission geometry measurements. The MR images from the two neonates were segmented into tissue types that included scalp, skull, gray brain matter, white brain matter, and ventricular and subarachnoidal CSF. Optical parameters used for the tissue types are tabulated in Table 1.

The DT images were coregistered with the anatomical images, and an affine transformation between the images was calculated in order to compensate for differences in geometric distortion between the modalities. This allows us to access the anisotropy data for any location in the anatomical model. To conserve the correctness of the directional information contained in the DT data under that spatial transformation, the tensor data were handled using the preservation of the principal direction algorithm.[18] Various tools documented in previous literature[19–21] were used to perform the spatial coregistrations and transformations.

We relate the diffusion tensor data, which describe the anisotropy of water diffusion, to optical anisotropy by assuming that the same anisotropic structures are behind both phenomena, and that the directional biases for water diffusion and photon migration are qualitatively similar.[7] This seems reasonable since measurements in chicken breast tissue show a preferential propagation of photons in the direction of the muscle fibers, which is also the preferential direction of the diffusion of water molecules.[2]

We use the fact that, in the case of diffusive photon propagation, the diffusion coefficient is approximately inversely proportional to the scattering coefficient. The scattering coefficient tensor $\mathbf{M}_s$ is calculated using the diffusion tensor $\mathbf{D}_{MRI}$ for water as[7]

$$\mathbf{M}_s = \frac{\mathbf{E}^T \mathbf{\Lambda}^{-1} \mathbf{E}}{\frac{1}{3} \, \mathrm{tr}(\mathbf{\Lambda}^{-1})}, \tag{5}$$

where $\mathbf{E}$ is a 3×3 matrix holding the eigenvectors of $\mathbf{D}_{MRI}$ as its columns, and $\mathbf{\Lambda}$ is a diagonal matrix with the corresponding eigenvalues as its diagonal elements. The normalization by $\frac{1}{3} \, \mathrm{tr}(\mathbf{\Lambda}^{-1})$ is chosen so that the average value of $\hat{\mathbf{s}}^T \mathbf{M}_s \hat{\mathbf{s}}$ integrated over the unit sphere is 1, giving an average scattering coefficient of $\mu_{s,iso}$.

C. Simulation Setup

Simulations were performed on the two infant head models using isotropic and anisotropic models. The two infants are referred to as infant I and infant II. For comparison, the significance of the correct modeling of the CSF region was studied by performing the simulations also in head models in which the optical properties of the CSF region had been replaced by the corresponding properties of gray brain matter.

To improve reconstruction results in optical tomography by using prior anatomical information, general anatomical models may need to be used since information from other imaging modalities of the subject or patient under study cannot be expected to always be available. The feasibility of a general anisotropy model was investigated by combining the anisotropy information of infant I with the anatomical information of infant II. An affine transformation was carried out to coregister the data sets. This was done by using a mutual information-based method[21] to coregister the FA map from the DT data of infant I to the anatomical data set of infant II. The coregistration result was carefully reviewed to verify a good match. The results using the correct anisotropy data of infant II and general data borrowed from the DT imaging of infant I were then compared. While using the anisotropy data simply borrowed from another individual is not equivalent to using a general atlas based on MR images from many individuals, the results thus obtained provide some insight into the feasibility of using such an atlas.

To investigate the implications of tissue anisotropy for different source–detector separations, we simulated measurements using a fiber array with one source and 20 detectors on the circumference of the head (see Fig. 2). The source and the detectors were placed on a transaxial plane approximately 1.5 cm above the upper end of the earlobes. The same setup was used in the simulations for the two head models. The signal intensity and phase shift seen by the detectors and the distribution of sensitivity for each measurement were calculated.

As a measure of how much the inclusion of the CSF and the anisotropy in the model of light propagation

Table 1. Optical Properties of Tissue Types[a]

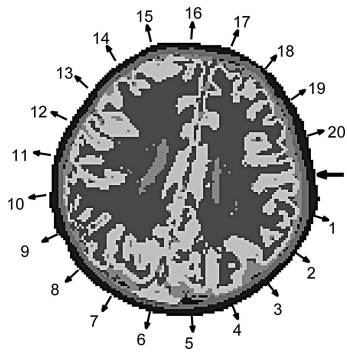| Tissue Type	μ_s (mm^{-1})	g	μ_a (mm^{-1})	n
Scalp	10	0.9	0.018	1.3
Skull	18	0.9	0.016	1.3
Gray matter	5	0.9	0.048	1.3
White matter	10	0.9	0.037	1.3
Subarachnoid CSF	0.027	0.9	0.0041	1.3
Ventricular CSF	0.01	0.9	0.0041	1.3

[a]Reference 9.

Fig. 2. Optode positions. The light source is shown as a large arrow pointing toward the center of the head, detectors numbered 1 through 20 are shown as smaller arrows pointing outward.

affect the predicted depth sensitivity within the head, the sensitivities to layers at different depths within the head model were calculated. We considered a layered structure consisting of three approximately 6 mm thick layers from the surface inward, with tissues deeper than 18 mm considered the fourth core layer. The boundaries of the three layers are shown for the two head models in Fig. 3. The figure also illustrates the very different head shapes of the two infants.

3. Results

The simulated exitance at the detectors was clearly different in the isotropic and anisotropic cases. Taking the anisotropy data into account increased the recorded signal intensity in all the detectors except those closest to the light source and reduced the phase shift of the measured signal in most detectors. The effect on signal intensity of the clear layer provided by the CSF, however, was greater than that of anisotropy. The effect of the CSF on the phase measurement type is also greater than that of anisotropy, though in the case of infant I, the difference is smaller. The intensity and phase responses for isotropic and anisotropic cases with and without the inclusion of the CSF in the model and the differences between anisotropic and isotropic cases are given in Fig. 4 for infant I and are given in Fig. 5 for infant II. Note that the intensity difference is given as a differ-
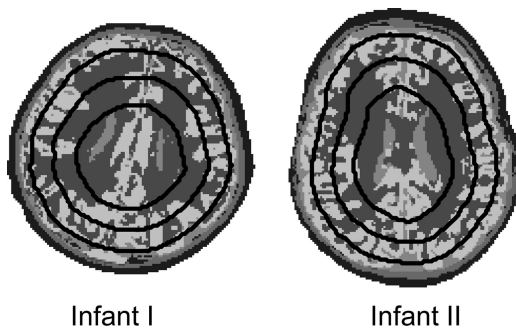

Fig. 3. Segmented head models of the two infants with borders of depth layers shown in black. Slices are taken at the level of the optical fibers.
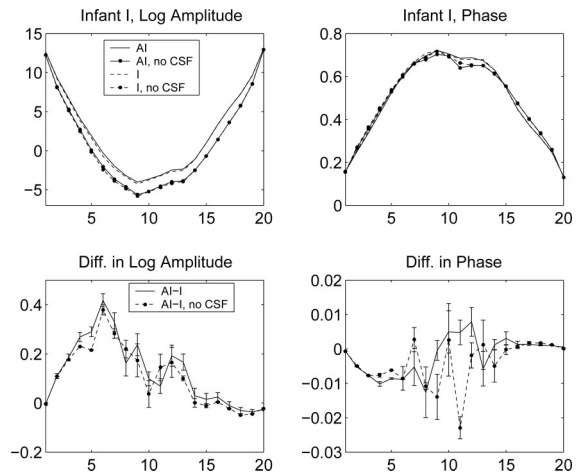

Fig. 4. Simulated measurement data for infant I. In the upper row, amplitude and phase response in the detectors on the circumference of the head. Anisotropic (AI) and isotropic (I) cases and the effect of inclusion of the CSF in the model are considered. In the lower row, differences in amplitude and phase responses between anisotropic and isotropic cases are shown for the case in which the CSF is taken into account and for the case in which it is not taken into account. Amplitude data are given in natural logarithmic scale (arbitrary units), phase response is given in radians. Error bars represent the standard deviation between different MC runs. The X-axis coordinate is the detector number.

ence in natural logarithm, and thus the maximum logarithmic differences of the order of 0.4 and 0.2 for infant I and infant II, respectively, correspond to differences of approximately 50% and 20% in signal intensity. The change in phase shift caused by an-
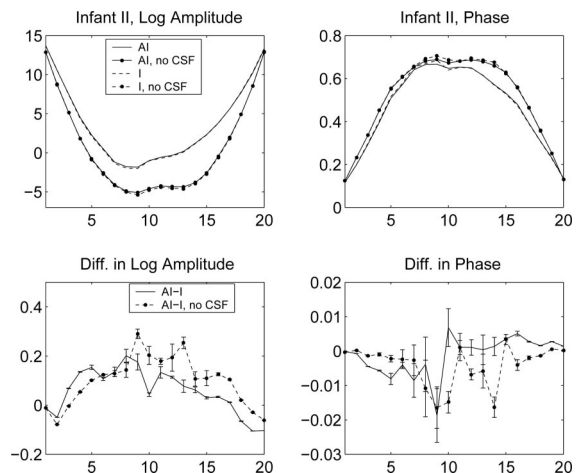

Fig. 5. Simulated measurement data for infant II. In the upper row, amplitude and phase response in the detectors on the circumference of the head. Anisotropic (AI) and isotropic (I) cases and the effect of inclusion of the CSF in the model are considered. In the lower row, differences in amplitude and phase responses between anisotropic and isotropic cases are shown for the case in which the CSF is taken into account and for the case in which it is not taken into account. Amplitude data are given in natural logarithmic scale (arbitrary units), phase response is given in radians. Error bars represent the standard deviation between different MC runs. The X-axis coordinate is the detector number.
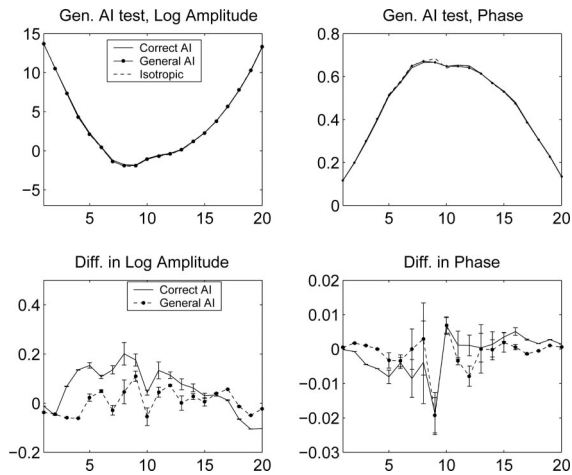
Fig. 6. Simulated measurement data for infant II using correct and general anisotropy models. In the upper row, amplitude and phase responses in detectors on the circumference of the head for the cases with correct and general anisotropy models and the isotropic case. In the lower row, the difference from the isotropic model is shown for the correct and general anisotropy models. Amplitude data are given in natural logarithmic scale (arbitrary units), phase response is given in radians. Error bars represent the standard deviation between different MC runs. The X-axis coordinate is the detector number.

isotropy is seen to be of the order of 2%–3% at maximum.

The results obtained using the general anisotropy model created by combining the DT data from infant I with the anatomical data from infant II are shown in Fig. 6. The graphs show a comparison between the isotropic model and the anisotropic models using the correct and general anisotropy. The effect of anisotropy is weaker when the borrowed general anisotropy data are used than when the correct anisotropy data are used. This seems reasonable as warping the anisotropy data of infant I to match the very different head shape of infant II altered some of the correspondence between the structures of the anatomical and anisotropy data. However, the general shape of the effect of anisotropy, as shown in the lower plots in Fig. 6, is similar when correct or general anisotropy data are used. The result suggests that using a general anisotropy model may be possible, but an atlas with average anisotropy data for different head shapes and gestational ages may be needed in order to accurately model the effect of anisotropy.

Our simulation results demonstrate that anisotropy and the CSF region clearly affect the measured optical signal. However, the effect of these considerations on the pattern of sensitivity to measurement is more important from the point of view of reconstructing the optical properties or functional changes in the brain. The sensitivity distributions from two source–detector pairs are shown in Fig. 7. The two measurements are selected so that light propagation between the source–detector pair shown in Fig. 7(a) is not along a major white matter bundle, whereas a significant part of the light propagation between the
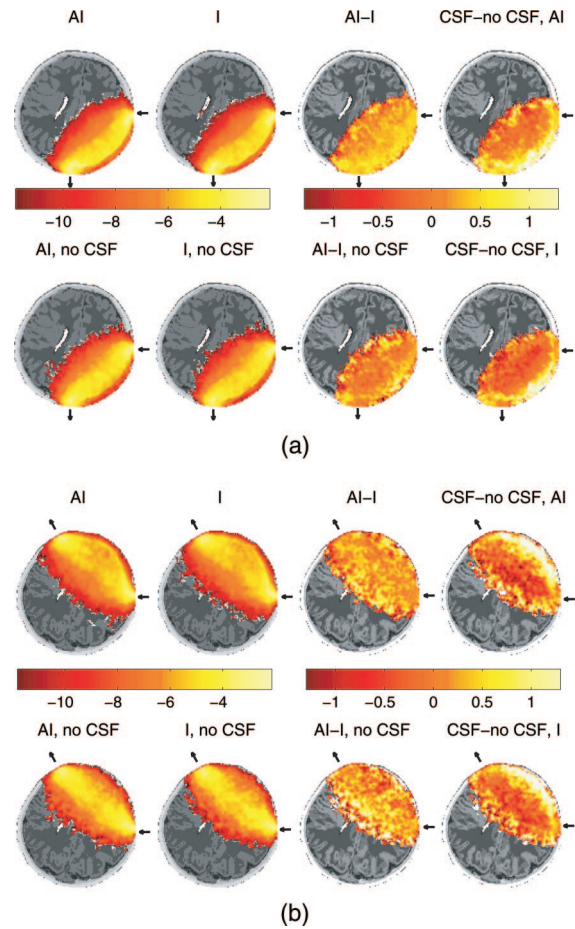

Fig. 7. Spatial distribution of sensitivity of a measurement between two source–detector pairs (a) and (b). The source and detector are indicated by arrows entering and exiting the head. Natural logarithm of scaled sensitivity $\ln [(\partial A/\partial \Delta \mu_s)/A]$ is shown. Sensitivity was calculated per cubical tissue element (0.6 mm side length), unit is millimeters. AI and I cases are shown with and without inclusion of the CSF in the model. In difference images, the difference in the logarithm of the scaled intensity is shown.

source–detector pair shown in Fig. 7(b) is along the direction of the white matter tracts of the corpus callosum. Sensitivity is shown for anisotropic and isotropic cases and for cases with and without the CSF layer.

The value of sensitivity was calculated for each cubical voxel element (side length of 0.6 mm) of the tissue model. Since anisotropy and the presence of a CSF layer affect the recorded signal intensity, the sensitivity was scaled by the intensity seen by the detector. Thus the sensitivity distributions shown are directly comparable. To illustrate differences between the cases, the difference in the spatial distribution of relative sensitivity between anisotropic and isotropic cases is shown as well as the difference between cases with and without the CSF layer.

Looking at the logarithmic sensitivity distributions shown in the four left-hand side images in Fig. 7, a small shift toward the surface of the head caused by the presence of the CSF can be seen, while the anisotropic and isotropic cases look more similar. How-

ever, looking at the images of the difference in logarithmic sensitivity between the anisotropic and the isotropic cases and between the cases with and without the CSF, differences become clearer. As shown in various previous publications (see, for example, Ref. 22), the presence of the CSF layer considerably reduces sensitivity to the regions below the CSF layer and increases sensitivity to the region in its immediate vicinity. Interestingly, the effect of anisotropy on the sensitivity to deeper tissues seems to vary between different source–detector pairs. For the case shown in Fig. 7(a) in which the source is at the side of the head near the earlobe, and the detector optode is placed at the back of the head, anisotropy increases the relative sensitivity to superficial tissue. In the case shown in Fig. 7(b) where the source is at the same position as in the previous case, but the detector optode is located on the forehead toward the opposite side of the head from the source, anisotropy seems to increase sensitivity to deeper tissue.

This result can be understood by considering the structure of the anisotropic white matter tracts. In cases where the source and detector are close to brain regions connected by strong white matter tracts, sensitivity along these tracts is enhanced, giving increased sensitivity to deeper tissue. This is the case for the source–detector pair in Fig. 7(b) in which the corpus callosum plays such a role. On the other hand, when the configuration of the white matter tracts is such that no strong white matter tract connects the region of the source to the region of the detector, the

effect, which may be more neutral or even increase in relative sensitivity to superficial tissues, can be seen. This is the case of the source–detector pair shown in Fig. 7(a). As illustrated in both cases presented in Fig. 7, the effect of the CSF on the sensitivity profile is greater than that of the anisotropy, but the effect of the anisotropy is strong enough to be seen on the same magnitude scale with the effect of the CSF. It is also worth noting that the inclusion of anisotropy in the model seems to modify the effect caused by the CSF as can be seen in the right-hand side difference images in Fig. 7(a).

The general effect of anisotropy on the sensitivity of the measurements at different depths was investigated by considering a layered structure consisting of three 6 mm thick shells and a core layer. The structure was described above and is illustrated in Fig. 3. The overall sensitivity to a specific depth was calculated as the summed sensitivity in a layer at that depth within the head model seen by a subgroup of the 20 detectors used in the simulation. The subgroups were chosen so as to see the effects in different parts of the head. Using the detector numbering presented in Fig. 2, the groups were chosen as follows. The detector group 1 consists of detectors 5 through 7 at the back of the head, around the sagittal midline. The detector group 2 consists of detectors 9 through 12 at the side of the head approximately opposite to the light source, and the detector group 3 consists of detectors 14 through 16 on the forehead.

Table 2. Relative Sensitivity to Different Depths by the Detector Group[a]

Detector Group 1	Depth up to 6 mm		Depth up to 12 mm		Depth up to 18 mm		Core	
	I	II	I	II	I	II	I	II
AI:	0.372	0.345	0.445	0.407	0.142	0.160	0.041	0.089
I:	0.371	0.342	0.438	0.412	0.147	0.161	0.044	0.065
AI-I (%):	0.2	1.0	1.6	−1.3	−3.3	−0.7	−6.7	3.7
No CSF:	0.325	0.194	0.431	0.392	0.184	0.271	0.060	0.144
CSF–no CSF (%):	14.6	78.0	3.1	3.7	−22.8	−40.9	−31.6	−38.4

Detector Group 2	Depth up to 6 mm		Depth up to 12 mm		Depth up to 18 mm		Core	
	I	II	I	II	I	II	I	II
AI:	0.268	0.414	0.262	0.309	0.204	0.145	0.265	0.131
I:	0.270	0.421	0.253	0.313	0.202	0.143	0.275	0.123
AI-I (%):	−0.6	−1.7	3.8	−1.1	0.8	1.8	−3.5	0.4
No CSF:	0.232	0.165	0.260	0.243	0.226	0.259	0.282	0.333
CSF–no CSF (%):	15.8	151.1	0.7	27.3	−9.8	−43.9	−5.8	−60.6

Detector Group 3	Depth up to 6 mm		Depth up to 12 mm		Depth up to 18 mm		Core	
	I	II	I	II	I	II	I	II
AI:	0.641	0.496	0.295	0.415	0.054	0.069	0.009	0.019
I:	0.642	0.511	0.297	0.405	0.052	0.066	0.009	0.018
AI-I (%):	−0.2	−2.9	−0.6	2.5	5.5	5.0	−0.5	8.1
No CSF:	0.548	0.278	0.352	0.480	0.085	0.188	0.016	0.054
CSF–no CSF (%):	17.0	78.4	−16.0	−13.5	−35.9	−63.2	−40.3	−64.5

[a]Relative sensitivities for different layers for infant I are shown in columns marked I and for infant II in columns marked II. The rows marked AI and I show data obtained using anisotropic and isotropic models, and rows marked No CSF show data obtained using a model in which the CSF is not considered. Percentual increase or decrease in sensitivity caused by the inclusion of anisotropy and the CSF in the model are given on rows marked AI-I and CSF–no CSF, respectively. Data for three detector groups are given.

The sensitivity values obtained were scaled so that the sum of sensitivities to all four regions was 1.0 for all detector groups, giving as a result, the relative sensitivities to the different layers for each detector group.

As can be seen from Fig. 3, the two infants have very different head shapes, which is reflected in different average photon penetration depths and depth sensitivities for similar source–detector arrays.

The relative sensitivities to different depths for the two head geometries are tabulated in Table 2. Sensitivity to the different layers is given for anisotropic and isotropic cases and for the case in which the CSF has been excluded from the model.

Results confirm that the effect of the CSF generally shifts sensitivity toward the more superficial tissues. The difference between the model including the CSF and the model without the CSF is large, with inclusion of the CSF in the model increasing the sensitivity of measurement to a layer even by more than 100%. This suggests that correct modeling of the CSF is very important for the successful localization of changes in blood volume or oxygenation using optical tomography. The inclusion of anisotropy in the model seems to shift the summed sensitivity of detector group 1 at the back of the head toward superficial tissues, and sensitivity of detector group 3 at the forehead toward deeper tissues in the case of infant I. This is consistent with the sensitivity maps presented in Fig. 7. However, the effect is small compared to the effect of inclusion of the CSF. The maximal change caused by anisotropy to the relative sensitivity to tissues at different depths was found to be of the order of a few percent.

4. Discussion

We have investigated the effect of tissue anisotropy in the DOT of newborn infants. We show that tissue anisotropy may have a noticeable effect on the signal obtained in optical imaging and, more importantly, also the pattern of sensitivity of the optical measurement is altered by the effect of anisotropy. However, the effect of anisotropy is small compared to that of the nonscattering region of cerebrospinal fluid.

The feasibility of using a general anisotropy model based on a general atlas of anisotropy data was studied using the anisotropy data of one individual and the anatomical data of another individual together. It was found that the effect obtained using this combination of data sets from different individuals was similar in shape to that obtained using the original anisotropy data, but the agreement was not perfect. The result suggests that improving the accuracy of modeling of photon propagation using a general anisotropy atlas may be possible, but probably average anisotropy models for different gestational ages would be required.

The treatise presented here is based on the model of anisotropy presented in Ref. 7, and the assumption that anisotropy in propagation of near-infrared photons and anisotropy of diffusion of water molecules shown in DT-MRI are related to each other. The assumption seems reasonable since tubelike structures that guide water molecules have also been shown to cause anisotropy in the propagation of photons.[2]

We have studied anisotropic effects in infant head models whose sizes correspond in size to a preterm infant and are small enough to allow transillumination. For long source–detector distances, the effect of anisotropy is almost exclusively due to the anisotropy of white matter tracts that is similar in preterm and full-term infants.[8] Therefore the results obtained can be assumed to hold for newborn infants in general. In the case of shorter source–detector distances, the larger tissue anisotropy present in the gray matter of the brains of preterm infants may have an effect that is not taken into account by this study. Therefore for shorter distances the results can be expected to be more accurate for full-term infants than for preterm infants.

References

1. M. Schweiger, S. R. Arridge, M. Hiraoka, and D. T. Delpy, "Application of the finite element method for the forward model in infrared absorption imaging," in *Mathematical Methods in Medical Imaging,* D. C. Wilson and J. N. Wilson, eds., Proc. SPIE **1768,** 97–108 (1992).
2. G. Marquez, L.-H. Wang, S.-P. Lin, J. A. Schwartz, and S. L. Thomsen, "Anisotropy in the absorption and scattering spectra of chicken breast tissue," Appl. Opt. **37,** 798–804 (1998).
3. S. Nickell, M. Hermann, M. Essenpreis, T. J. Farrell, U. Krämer, and M. S. Patterson, "Anisotropy of light propagation in human skin," Phys. Med. Biol. **45,** 2873–2886 (2000).
4. A. Kienle, F. K. Forster, R. Diebolder, and H. Hibst, "Light propagation in dentin: influence of microstructure on anisotropy," Phys. Med. Biol. **48,** N7–N14 (2003).
5. J. Heino, S. Arridge, J. Sikora, and E. Somersalo, "Anisotropic effects in highly scattering media," Phys. Rev. E **68,** 031908 (2003).
6. L. Dagdug, G. H. Weill, and A. H. Gandjbakhche, "Effects of anisotropic optical properties on photon migration in structured tissues," Phys. Med. Biol. **48,** 1361–1370 (2003).
7. J. Heiskala, I. Nissilä, T. Neuvonen, S. Järvenpää, and E. Somersalo, "Modeling anisotropic light propagation in a realistic model of the human head," Appl. Opt. **44,** 2049–2057 (2005).
8. R. C. McKinstry, A. Marthur, J. H. Miller, A. Ozcan, A. Z. Snyder, G. L. Schefft, C. R. Almli, S. I. Shiran, T. E. Conturo, and J. J. Neil, "Radial organization of developing preterm human cerebral cortex revealed by non-invasive water diffusion anisotropy MRI," Cereb. Cortex **12,** 1237–1243 (2002).
9. F. Schmidt, "Development of a time-resolved optical tomography system for neonatal brain imaging," Ph.D. dissertation (University of London, 1999).
10. S. A. Prahl, M. Keijzer, S. L. Jacques, and A. J. Welch, "A Monte Carlo model of light propagation in tissue," in *Dosime-*

try of Laser Radiation in Medicine and Biology, G. J. Müller and D. H. Sliney, eds. (SPIE IS, 1989), Vol. 5, pp. 102–111.

11. L. H. Wang, S. L. Jacques, and L.-Q. Zheng, "Monte Carlo modeling of photon transport in multilayered tissues," Comput. Methods Programs Biomed. **47,** 131–146 (1995).

12. D. A. Boas, J. P. Culver, J. J. Stott, and A. K. Dunn, "Three dimensional Monte Carlo code for photon migration through complex heterogenous media including the adult human head," Opt. Express **10,** 159–170 (2002).

13. C. K. Hayakawa, J. Spanier, F. Bevilacqua, A. K. Dunn, J. S. You, B. J. Tromberg, and V. Venugopalan, "Perturbation Monte Carlo methods to solve inverse photon migration problems in heterogeneous tissues," Opt. Lett. **26,** 1335–1337 (2001).

14. J. Spanier and E. M. Gelbardm, *Monte Carlo Principles and Neutron Transport Problems* (Addison-Wesley, 1969).

15. Y. Phaneendra Kumar and R. M. Vasu, "Reconstruction of optical properties of low-scattering tissue using derivative estimated through perturbation Monte-Carlo method, J. Biomed. Opt. **9,** 1002–1012 (2004).

16. General Electric Company, 3135 Easton Turnpike, Fairfield, Conn. 06828-0001.

17. P. J. Basser and C. Pierpaoli, "Microstructural and physiolog-ical features of tissues elucidated by quantitative-diffusion-tensor MRI," J. Magn. Reson. Ser B **111,** 209–219 (1996).

18. D. C. Alexander, C. Pierpaoli, P. J. Basser, and J. C. Gee, "Spatial transformations of diffusion tensor magnetic resonance images," IEEE Trans. Med. Imaging **20,** 1131–1139 (2001).

19. S. J. Kiebel, J. Ashburner, J. B. Poline, and K. J. Friston, "MRI and PET coregistration—a cross validation of statistical parametric mapping and automated image registration," Neuroimage **5,** 271–279 (1997).

20. M. Jenkinson and S. Smith, "A global optimisation method for robust affine registration of brain images," Med. Image Anal. **5,** 143–156 (2001).

21. K. Van Leemput and J. Hämäläinen, "A cross-platform software framework for medical image processing," in *Proceedings of the Seventh International Conference on Medical Image Computing and Computer-Assisted Intervention (MICCAI),* Part II (Springer, 2004), pp. 1091–1092.

22. E. Okada, M. Firbank, M. Schweiger, S. R. Arridge, M. Cope, and D. T. Delpy, "Theoretical and experimental investigation of near-infrared light propagation in a model of the adult head," Appl. Opt. **36,** 21–31 (1997).

23. Biomediucm Bioinformatics Unit, Haartmaninkatu 8, FIN-00290 Helsinki, Finland, http://home.bioinfo.helsinki.fi.